








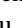





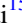



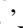

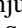

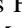



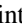
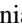


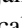



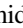





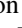



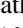






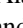







Precise Transit and Radial-velocity Characterization of a Resonant Pair: The Warm Jupiter TOI-216c and Eccentric Warm Neptune TOI-216b

Rebekah I. Dawson¹ , Chelsea X. Huang^{2,36} , Rafael Brahm^{3,4} , Karen A. Collins⁵ , Melissa J. Hobson^{4,6} , Andrés Jordán^{3,4} , Jiayin Dong^{1,7} , Judith Korth⁸ , Trifon Trifonov⁹ , Lyu Abe¹⁰ , Abdelkrim Agabi¹⁰ , Ivan Bruni¹¹ , R. Paul Butler¹² , Mauro Barbieri¹³ , Kevin I. Collins¹⁴ , Dennis M. Conti¹⁵ , Jeffrey D. Crane¹⁶ , Nicolas Crouzet¹⁷ , Georgina Dransfield¹⁸ , Phil Evans¹⁹ , Néstor Espinoza²⁰ , Tianjun Gan²¹ , Tristan Guillot¹⁰ , Thomas Henning⁹ , Jack J. Lissauer²² , Eric L. N. Jensen²³ , Wenceslas Marie Sainte²⁴ , Djamel Mékarnia¹⁰ , Gordon Myers²⁵ , Sangeetha Nandakumar¹³ , Howard M. Relles⁵ , Paula Sarkis⁹ , Pascal Torres^{4,6} , Stephen Shtetman¹⁶ , François-Xavier Schmider¹⁰ , Avi Shporer² , Chris Stockdale²⁶ , Johanna Teske^{16,37} , Amaury H. M. J. Triaud¹⁸ , Sharon Xuesong Wang¹⁶ , Carl Ziegler²⁷ , G. Ricker² , R. Vanderspek² , David W. Latham⁵ , S. Seager^{2,28,29} , J. Winn³⁰ , Jon M. Jenkins²² , L. G. Bouma³⁰ , Jennifer A. Burt³¹ , David Charbonneau⁵ , Alan M. Levine² , Scott McDermott³² , Brian McLean³³ , Mark E. Rose²² , Andrew Vanderburg^{34,38} , and Bill Wohler^{22,35} 

¹ Department of Astronomy & Astrophysics, Center for Exoplanets and Habitable Worlds, The Pennsylvania State University, University Park, PA 16802, USA
rdawson@psu.edu

² Department of Physics and Kavli Institute for Astrophysics and Space Research, Massachusetts Institute of Technology, Cambridge, MA 02139, USA

³ Facultad de Ingeniería y Ciencias, Universidad Adolfo Ibáñez, Av. Diagonal las Torres 2640, Peñalolén, Santiago, Chile

⁴ Millennium Institute for Astrophysics, Chile

⁵ Harvard-Smithsonian Center for Astrophysics, 60 Garden Street, Cambridge, MA 02138, USA

⁶ Instituto de Astrofísica, Facultad de Física, Pontificia Universidad Católica de Chile, Chile

⁷ Center for Computational Astrophysics, Flatiron Institute, 162 Fifth Avenue, New York, NY 10010, USA

⁸ Rheinisches Institut für Umweltforschung, Abteilung Planetenforschung an der Universität zu Köln, Universität zu Köln, Aachenerstraße 209, D-50931 Köln, Germany

⁹ Max Planck Institute for Astronomy, Königstuhl 17, D-69117 Heidelberg, Germany

¹⁰ Université Côte d'Azur, Observatoire de la Côte d'Azur, CNRS, Laboratoire Lagrange Bd de l'Observatoire, CS 34229, F-06304 Nice Cedex 4, France

¹¹ INAF OAS, Osservatorio di Astrofisica e Scienza dello Spazio di Bologna via Piero Gobetti 93/3, Bologna, Italy

¹² Carnegie Institution for Science, Earth & Planets Laboratory, 5241 Broad Branch Road NW, Washington, DC 20015, USA

¹³ INCT, Universidad de Atacama, calle Copayapu 485, Copiapó, Atacama, Chile

¹⁴ George Mason University, 4400 University Drive, Fairfax, VA 22030 USA

¹⁵ American Association of Variable Star Observers, 49 Bay State Road, Cambridge, MA 02138, USA

¹⁶ Observatories of the Carnegie Institution for Science, 813 Santa Barbara Street, Pasadena, CA 91101, USA

¹⁷ European Space Agency (ESA), European Space Research and Technology Centre (ESTEC), Keplerlaan 1, 2201 AZ Noordwijk, The Netherlands

¹⁸ University of Birmingham, School of Physics & Astronomy, Edgbaston, Birmingham B15 2TT, UK

¹⁹ El Sauce Observatory, Coquimbo Province, Chile

²⁰ Space Telescope Science Institute, 3700 San Martin Drive, Baltimore, MD 21218, USA

²¹ Department of Astronomy, Tsinghua University, Beijing 100084, People's Republic of China

²² NASA Ames Research Center, Moffett Field, CA 94035, USA

²³ Department of Physics & Astronomy, Swarthmore College, Swarthmore PA 19081, USA

²⁴ Institut Paul Emile Victor, Concordia Station, Antarctica

²⁵ AAVSO, 5 Inverness Way, Hillsborough, CA 94010, USA

²⁶ Hazelwood Observatory, Australia

²⁷ Dunlap Institute for Astronomy and Astrophysics, University of Toronto, 50 St. George Street, Toronto, Ontario M5S 3H4, Canada

²⁸ Department of Earth, Atmospheric, and Planetary Sciences, Massachusetts Institute of Technology, Cambridge, MA 02139, USA

²⁹ Department of Aeronautics and Astronautics, Massachusetts Institute of Technology, Cambridge, MA 02139, USA

³⁰ Department of Astrophysical Sciences, Princeton University, 4 Ivy Lane, Princeton, NJ 08540, USA

³¹ Jet Propulsion Laboratory, California Institute of Technology, 4800 Oak Grove Drive, Pasadena, CA 91109, USA

³² Proto-Logic LLC, 1718 Euclid Street NW, Washington, DC 20009, USA

³³ Mikulski Archive for Space Telescopes, Space Telescope Science Institute, 3700 San Martin Drive, Baltimore, MD 21218, USA

³⁴ Department of Astronomy, The University of Texas at Austin, Austin, TX 78712, USA

³⁵ SETI Institute, Mountain View, CA 94043, USA

Received 2020 July 31; revised 2020 December 12; accepted 2021 January 4; published 2021 March 4

Abstract

TOI-216 hosts a pair of warm, large exoplanets discovered by the TESS mission. These planets were found to be in or near the 2:1 resonance, and both of them exhibit transit timing variations (TTVs). Precise characterization of the planets' masses and radii, orbital properties, and resonant behavior can test theories for the origins of planets orbiting close to their stars. Previous characterization of the system using the first six sectors of TESS data suffered from a degeneracy between planet mass and orbital eccentricity. Radial-velocity measurements using HARPS, FEROS, and the Planet Finder Spectrograph break that degeneracy, and an expanded TTV baseline from TESS and an ongoing ground-based transit observing campaign increase the precision of the mass and eccentricity measurements. We determine that TOI-216c is a warm Jupiter, TOI-216b is an eccentric warm Neptune, and that they librate in 2:1 resonance with a moderate libration amplitude of 60^{+2}_{-2} deg, a small but significant free

³⁶ Juan Carlos Torres Fellow.

³⁷ NASA Hubble Fellow.

³⁸ NASA Sagan Fellow.

eccentricity of $0.0222^{+0.0005}_{-0.0003}$ for TOI-216b, and a small but significant mutual inclination of $1^{\circ}2\text{--}3^{\circ}9$ (95% confidence interval). The libration amplitude, free eccentricity, and mutual inclination imply a disturbance of TOI-216b before or after resonance capture, perhaps by an undetected third planet.

Unified Astronomy Thesaurus concepts: [Exoplanet astronomy \(486\)](#); [Exoplanet dynamics \(490\)](#); [Transit timing variation method \(1710\)](#); [Radial velocity \(1332\)](#)

1. Introduction

Warm Jupiters—defined here as giant planets with 10–100 day orbital periods—in systems with other nearby planets are an important population for the investigation of giant planets close to their stars. High-eccentricity tidal migration—a strong contender for the origins of many close-in giant planets (see Dawson & Johnson 2018 for a review)—is unlikely to have been at work in these systems (e.g., Mustill et al. 2015). Disk migration has been a persistently proposed explanation (e.g., Lee & Peale 2002)—particularly for systems in or near mean motion resonance—but recent studies have argued that in situ formation may be more consistent with these planets’ observed properties (e.g., Huang et al. 2016; Frelih et al. 2019; Anderson et al. 2020) and could possibly be consistent with resonant configurations (e.g., Dong & Dawson 2016; MacDonald & Dawson 2018; Choksi & Chiang 2020; Morrison et al. 2020). Precise characterization of the orbital properties and resonant behavior of individual systems can test origin scenarios, complementary to population studies.

One warm Jupiter system potentially amenable to such detailed characterization is TOI-216, which hosts a pair of warm, large exoplanets discovered by the TESS mission (Dawson et al. 2019; Kipping et al. 2019). Their masses and orbits were characterized using transit timing variations (TTVs). However, previously, the TESS TTV data set was not sufficiently precise to break the degeneracy between mass and eccentricity that arises when we can measure the near-resonant TTV signal but not the chopping TTV signal (e.g., Lithwick & Naoz 2011; Deck & Agol 2015). Different priors on mass and eccentricity led to two qualitatively different solutions for the system (Dawson et al. 2019): a Jupiter-mass planet accompanied by a Saturn-mass planet librating in orbital resonance, and a puffy sub-Saturn-mass planet and puffy Neptune-mass planet near but not in orbital resonance. The solutions also differed in the planets’ free eccentricity, the eccentricity not associated with the proximity to resonance. Because any origin scenario under consideration needs to be able to account for the planets’ masses, free eccentricities, and resonant behavior, a detailed characterization of these properties with a more extended data set is warranted.

Since our previous study (Dawson et al. 2019), seven more TESS transits of planet b, three more TESS transits of planet c, a ground-based transit of planet b, and five more ground-based transits of planet c have been observed, including recent ground-based transit observations that significantly extend the baseline for measuring TTVs beyond the observations conducted during the first year of the TESS primary mission. Furthermore, we have been conducting a ground-based radial-velocity campaign using HARPS, FEROS, and the Planet Finder Spectrograph (PFS). Radial-velocity measurements serve to break the mass–eccentricity degeneracy.

Here we combine TESS light curves, ground-based light curves, and ground-based radial velocities to precisely characterize TOI-216b and c. In Section 2, we describe our

analysis of the TESS data and the observation and analysis of ground-based light curves. We identify a weak stellar activity periodicity in the TESS data that also shows up in the radial velocities. In Section 3, we present radial-velocity measurements from HARPS, FEROS, and PFS and show that they immediately confirm the higher-mass, lower-eccentricity solution. We investigate additional weak periodicities in the radial velocities and argue that they are caused by stellar activity. We jointly fit the TTVs and radial velocities in Section 4 and determine that the planet pair is librating in resonance, that the inner planet has a significant free eccentricity, and that planets have a small but significant mutual inclination. We present our conclusions—including implications for the system’s origins—in Section 5.

2. Light-curve Analysis

This paper is based on data from TESS Sectors 1–13 (2018 July 25–2019 July 17) and Sectors 27–30 (2020 July 4–2020 October 21), during which TOI-216 was observed with CCD 1 on Camera 4 and from ground-based observatories. We use the publicly available 2 minute cadence TESS data, which is processed with the Science Processing Operations Center pipeline (Jenkins et al. 2016). We download the publicly available data from the Mikulski Archive for Space Telescopes (MAST). The pipeline, a descendant of the Kepler mission pipeline based at the NASA Ames Research Center (Jenkins et al. 2002, 2010), analyzes target pixel postage stamps that are obtained for preselected target stars.

We use the resources of the TESS Follow-up Observing Program (TFOP) Working Group (WG) Sub Group 1 (SG1)³⁹ to collect seeing-limited time-series photometric follow-up of TOI-216. All photometric time series are publicly available on the Exoplanet Follow-up Observing Program for TESS (ExoFOP-TESS) website.⁴⁰ Light curves observed on or before 2019 February 24 are described in Dawson et al. (2019). Our new time-series follow-up observations are listed in Table 1. We used the TESS Transit Finder, which is a customized version of the Tapir software package (Jensen 2013), to schedule our transit observations. Unless otherwise noted, the photometric data were extracted using the AstroImageJ (AIJ) software package (Collins et al. 2017). The facilities used to collect the new TOI-216 observations published here are the Las Cumbres Observatory Global Telescope (LCOGT) network (Brown et al. 2013), Hazelwood Observatory (Churchill, Vic, Australia), El Sauce Observatory (Coquimbo Province, Chile), and the Antarctic Search for Transiting Exoplanets (ASTEP) observatory (Concordia Station, Antarctica). All LCOGT 1 m telescopes are equipped with the Sinistro camera, with a $4k \times 4k$ pixel Fairchild back-illuminated CCD and a $26' \times 26'$ field of view. The LCOGT images were calibrated using the standard LCOGT BANZAI pipeline (McCully et al. 2018). Hazelwood is a private observatory

³⁹ <https://tess.mit.edu/followup/>

⁴⁰ <https://exofop.ipac.caltech.edu/tess/>

Table 1
Observation Log: TOI-216/TIC 55652896

TOI-216	Date (UTC)	Telescope ^a	Filter	ExpT (seconds)	Exp (<i>N</i>)	Dur. (minutes)	Transit Coverage	Ap. Radius (arcseconds)	FWHM (arcseconds)
b	2019-10-30	LCOGT-CTIO-1.0	<i>I</i>	40	220	241	Full	5.8	2.4
	2020-05-23	ASTEP-0.4	$\sim Rc$	120	376	924	Full	10.2	5.3
c	2018-12-16	LCOGT-SAAO-1.0	<i>i'</i>	90	331	450	Full	5.8	2.1
	2019-01-20	Hazelwood-0.3	<i>g'</i>	240	101	449	Egress+70%	5.5	3.2
	2019-02-24	El Sauce-0.36	<i>Rc</i>	30	514	303	Egress+90%	5.9	3.4
	2019-06-07	ASTEP-0.4	$\sim Rc$	120	549	1440	Full	12.0	5.0
	2019-11-27	Hazelwood-0.3	<i>Rc</i>	60	114	255	Egress+60%	5.5	3.1
	2019-12-31	LCOGT-SAAO-1.0	<i>Ic</i>	40	316	345	Ingress+90%	4.7	2.0
	2020-02-24	Hazelwood-0.3	<i>Rc</i>	120	161	380	Egress+60%	5.5	3.1
	2020-03-09	LCOGT-CTIO-1.0	<i>I</i>	40	146	176	Egress+30%	8.2	2.6
	2020-06-21	ASTEP-0.4	$\sim Rc$	120	272	656	Full	11.0	5.0

Note.

^a Telescopes: LCOGT-CTIO-1.0: Las Cumbres Observatory—Cerro Tololo Inter-American Observatory (1.0 m) LCOGT-SAAO-1.0: Las Cumbres Observatory—South African Astronomical Observatory (1.0 m) LCOGT-SSO-1.0: Las Cumbres Observatory—Siding Spring Observatory (1.0 m) Hazelwood-0.3: Stockdale Private Observatory—Victoria, Australia (0.32 m) El Sauce-0.36: El Sauce Observatory—Coquimbo Province, Chile (0.36 m) ASTEP-0.4: Antarctic Search for Transiting Exoplanets—Concordia Station, Antarctica (0.4 m).

with an *f*/8 Planewave Instruments CDK12 0.32 m telescope and an SBIG STT3200 $2.2k \times 1.5k$ CCD, giving a $20' \times 13'$ field of view. El Sauce is a private observatory that hosts a number of telescopes; the observations reported here were carried out with a Planewave Instruments CDK14 0.36 m telescope and an SBIG STT-1603-3 $1536k \times 1024k$ CCD, giving a $19' \times 13'$ field of view. ASTEP is a 0.4 m telescope with an FLI Proline 16801E $4k \times 4k$ CCD, giving a $63' \times 63'$ field of view. The ASTEP photometric data were extracted using a custom IDL-based pipeline.

We fit the transit light curves (Figure 1) using the TAP software package (Gazak et al. 2012), which implements Markov Chain Monte Carlo (MCMC) using the Mandel & Agol (2002) transit model and the Carter & Winn (2009) wavelet likelihood function, with the modifications described in Dawson et al. (2014). The results are summarized in Table 2 and Table 3. For TESS light curves, we use the presearch data-conditioned flux, which is corrected for systematic (e.g., instrumental) trends using cotrending basis vectors (Smith et al. 2012; Stumpe et al. 2014). For all light curves, we use the Carter & Winn (2009) wavelet likelihood function (which, for the red noise component, assumes noise with an amplitude that scales as frequency⁻¹) with free parameters for the amplitude of the red σ_r and white noise σ_w and a linear trend fit simultaneously to each transit light-curve segment with other transit parameters. For the ground-based observations, we fit a linear trend to airmass instead of time. We assign each instrument and filter (TESS, Hazelwood *g'* and *Rc*, LCOGT *i'* and *I*, El Sauce *Rc*, and ASTEP *Rc*) its own set of limb-darkening parameters because of the different wave bands. We use one set of noise parameters for all the TESS light curves and an additional set for each ground-based light curve. We adopt uniform priors on the planet-to-star radius ratio (R_p/R_*), the impact parameter *b* (which can be either negative or positive; we report $|b|$), the midtransit time, the limb-darkening coefficients q_1 and q_2 (Kipping 2013), and the slope and intercept of each transit segment's linear trend. For the grazing transits of the inner planet, we impose a uniform prior on R_p/R_* from 0 to 0.17, with the upper limit corresponding to a planet radius of 0.13 solar radii (see Dawson et al. 2019 for details and justification). Despite a well-constrained transit depth

(Table 2), the inner planet's radius ratio is highly uncertain due to degeneracy between the radius ratio and impact parameter (see Figure 3 of Dawson et al. 2019). We also impose a uniform prior on the log of the light-curve stellar density ρ_{circ} . We use ρ_{circ} , the stellar density derived from the light curve assuming a circular orbit, to compute the Mandel & Agol (2002) model normalized separation of centers $z = d/R_*$, assuming $M_p \ll M_*$ and a circular orbit:

$$z = (\rho_{\text{circ}}/\rho_{\odot})^{1/3}(P/P_{\oplus})^{2/3}(a_{\oplus}/R_{\odot}) \quad (1)$$

where P is the orbital period, the subscript \oplus denotes Earth, and the subscript \odot denotes the Sun. We will later combine the posteriors ρ_{circ} from the light curve and ρ_* (from Dawson et al.'s 2019 isochrone fit) to constrain the orbital eccentricity (Section 4.2). We perform an additional set of fits where we allow for a dilution factor for the TESS light curves and find the results to be indistinguishable. We measure a dilution factor of $1.000^{+0.012}_{-0.011}$.

We also perform two additional fits to look for transit duration variations, following Dawson (2020). In the first fit, we allow the impact parameter to vary with the prior recommended by Dawson (2020). We find tentative evidence for the variation in the transit impact parameter for the inner planet, with an impact parameter change scale of $0.007^{+0.004}_{-0.003}$. In the second fit, we allow ρ_{circ} (Equation (1)) and *b* to vary for each transit with a prior that corresponds to a uniform prior in transit duration (Dawson 2020). Again, the inner planet exhibits tentative evidence for variation in its transit durations. We fit a line to the transit durations as a function of midtransit time and determine a 3σ confidence interval on the slope of -0.4 to 4 s day⁻¹ for the inner planet and -1 to 0.4 s day⁻¹ for the outer planet.

For comparison and to ensure that the results are not sensitive to the correlated noise treatment, we also fit the light curves using the `exoplanet` package (Foreman-Mackey et al. 2019), which uses Gaussian process regression. Each set of TESS light curves along with eight ground-based light curves is modeled with a light-curve transit model built from `starry` (Luger et al. 2019) plus a Matern-3/2 Gaussian process kernel with a white noise term. Seven sets of limb-

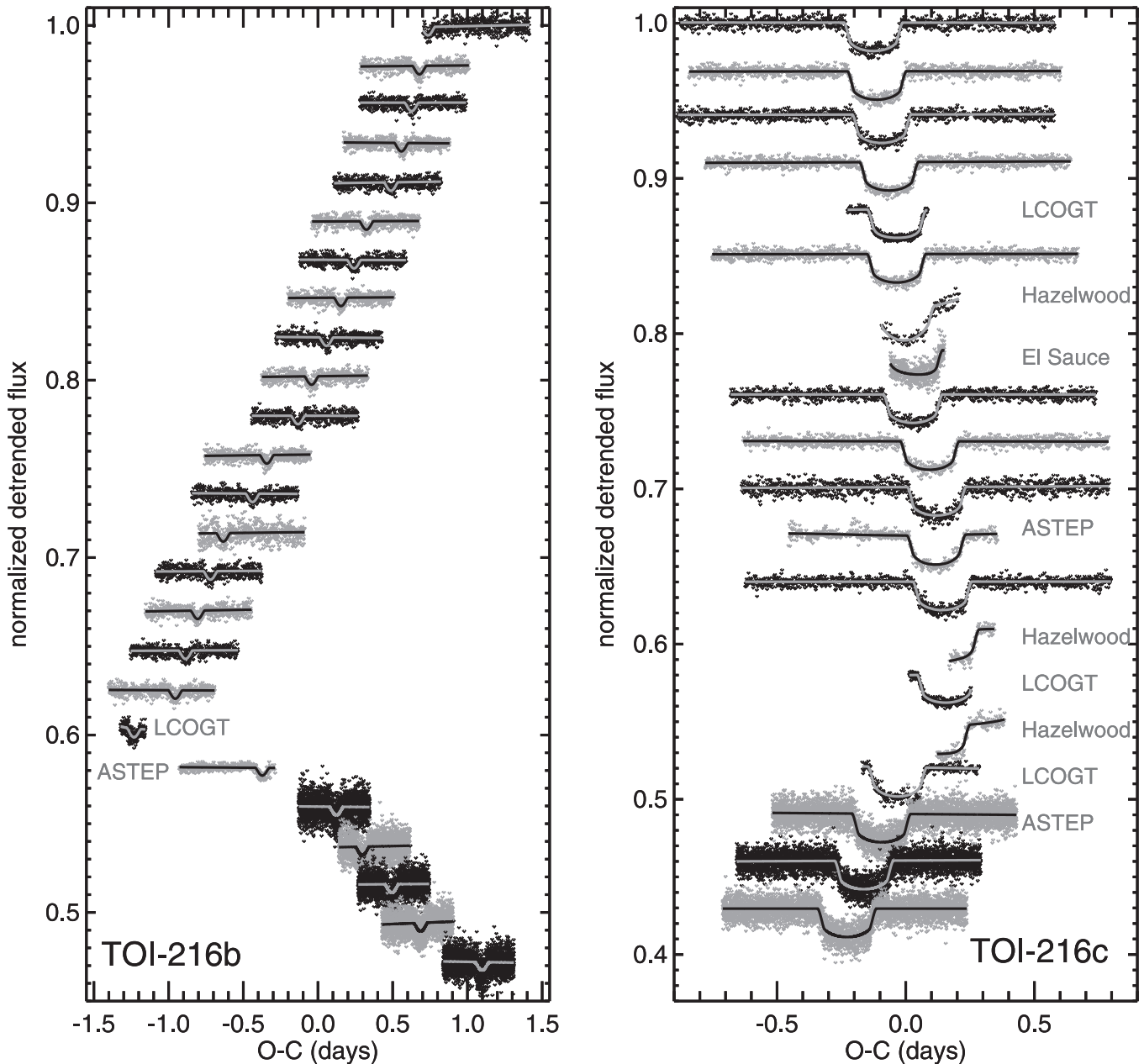


Figure 1. Detrended light curves, spaced with arbitrary vertical offsets, and with a model light curve overplotted. The light curves are phased based on a constant orbital period linear ephemeris to show the TTVs. TESS data are publicly available from MAST and ground-based data from the ExoFOP-TESS website.

darkening parameters (Kipping 2013) are used for observations conducted in seven different filters. We use a log-uniform prior on stellar densities (ρ_{circ}), log-normal prior on transit depths, uniform prior on the impact parameters, and uniform prior on midtransit times. We infer posteriors for each parameter using this approach that are consistent within 1σ to our nominal fit above.

We examine the light curve for evidence of stellar rotation. We do not see any significant periodicities in the SPOC 2 minute cadence data. To investigate further, we create a systematics-corrected long-cadence light curve using *eleanor* (Feinstein et al. 2019) with a 15×15 target pixel file, background size of 100, and custom square aperture of 3×3 pixels centered on TOI-216. We follow *eleanor*'s recommendation for background subtraction: the 1D postcard background for sectors 1, 2, 4, 6, 7, 8, 11, and 13; the 1D

target pixel file background for sectors 3 and 5; and the 2D target pixel file background for sectors 9 and 12. Then, we mask out the transits and compute a discrete autocorrelation function (DCF; Equation (2) of Edelson & Krolik 1988), plotted in Figure 2.

The peak at 6.5 days and the valley at approximately half that value are consistent with a 6.5 day periodicity. This periodicity could represent the rotation period or a shorter harmonic. A rotation period of ~ 10 – 40 days would be most typical for a $0.78 M_{\odot}$ star on the main sequence (e.g., McQuillan et al. 2014), so the periodicity could plausibly be an integer fraction of the rotation period (e.g., one half, one third). The stellar radius of $0.747^{+0.015}_{-0.014} R_{\odot}$ (Dawson et al. 2019) and $v \sin i = 0.84 \pm 0.70 \text{ km s}^{-1}$ from the FEROS spectra correspond to a rotation period of 45^{+225}_{-20} days assuming an edge-on orientation. A rotation period of 26 days would be compatible

Table 2
Planet Parameters for TOI-216b and TOI-216c Derived from the Light Curves

Parameter	Value ^a	
TOI-216b		
Planet-to-star radius ratio, R_p/R_*	0.10	+0.03 -0.02
Transit depth [ppm]	4750	+140 -150
Planet radius, R_p [R_\oplus]	8	+3 -2
Light curve stellar density ^b , ρ_{circ} [ρ_\odot]	1.1	+0.3 -0.2
Impact parameter, $ b $	0.98	+0.05 -0.04
Midtransit times (days) ^{c,d}	1325.328	+0.004 -0.004
	1342.430	+0.003 -0.003
	1359.540	+0.003 -0.003
	1376.631	+0.003 -0.003
	1393.723	+0.003 -0.003
	1427.879	+0.003 -0.003
	1444.958	+0.003 -0.003
	1462.031	+0.003 -0.003
	1479.094	+0.003 -0.003
	1496.155	+0.003 -0.003
	1513.225	+0.004 -0.004
	1547.338	+0.003 -0.003
	1564.403	+0.004 -0.004
	1598.529	+0.003 -0.003
	1615.604	+0.003 -0.003
	1632.679	+0.003 -0.003
	1649.759	+0.004 -0.004
	1666.851	+0.003 -0.003
LCOGT	1786.698	+0.002 -0.002
ASTEP	1993.486	+0.002 -0.002
	2045.465	+0.003 -0.003
	2062.800	+0.003 -0.003
	2080.157	+0.003 -0.003
	2097.511	+0.003 -0.003
	2132.243	+0.003 -0.003
Best-fit linear ephemeris:		
Period (days)	17.16073	
Epoch (days)	1324.5911	
TOI-216c		
Planet-to-star radius ratio, R_p/R_*	0.1230	+0.0008 -0.0006
Transit depth [ppm]	18310	+120 -120
Planet radius, R_p [R_\oplus]	10.1	+0.2 -0.2
Light-curve stellar density, ρ_{circ} [ρ_\odot]	1.73	+0.04 -0.08
Impact parameter, $ b $	0.14	+0.08 -0.09
Midtransit times (days) ^{c,d}	1331.2850	+0.0008 -0.0008
	1365.8244	+0.0008 -0.0008
	1400.3686	+0.0008 -0.0008
	1434.9227	+0.0008 -0.0008
	1469.4773	+0.0008 -0.0008
LCOGT	1469.4781	+0.0004 -0.0004
Hazelwood	1504.036	+0.002 -0.002
El Sauce	1538.5938	+0.0015 -0.0015
	1538.5921	+0.0008 -0.0008
	1607.7082	+0.0008 -0.0008
	1642.2612	+0.0009 -0.0009
ASTEP	1642.2595	+0.0011 -0.0011
	1676.8085	+0.0008 -0.0008
Hazelwood	1814.939	+0.003 -0.003
LCOGT	1849.4526	+0.0005 -0.0005
Hazelwood	1883.955	+0.002 -0.002
LCOGT	1918.4506	+0.0007 -0.0007
ASTEP	2021.8887	+0.0010 -0.0010

Table 2
(Continued)

Parameter	Value ^a	
	2056.3520	+0.0008 -0.0008
	2090.8107	+0.0009 -0.0009
	2125.2698	+0.0008 -0.0008
Best-fit linear ephemeris:		
Period (days)	34.525528	
Epoch (days)	1331.4110	

Notes.

^a As a summary statistic, we report the median and 68.3% confidence interval of the posterior distribution.

^b Equation (1).

^c BJD-2457000.0 days.

^d Midtransit times not otherwise noted are from TESS light curves.

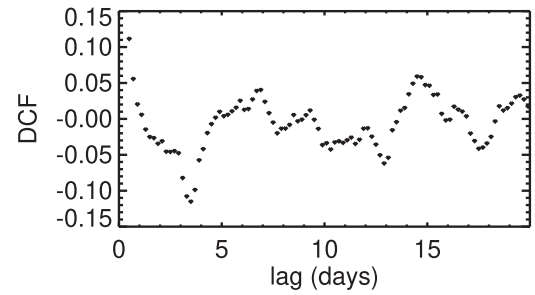


Figure 2. Discrete autocorrelation function (Equation (2) of Edelson & Krolik 1988) of the *eleanor* long-cadence TOI-216 light curve.

with the $v \sin i$ measurement, or a shorter rotation period would indicate a spin-orbit misalignment. A periodicity of 13 days or 26 days is challenging to detect in the TESS light curve (e.g., Canto Martins et al. 2020). Thirteen days is close to TESS’s 13.7 day orbital period and thus susceptible to corrections for systematics. Both are a significant fraction of the sector (27 days) and subject to imprecision in stitching together different segments. Given the many bumps and wiggles in the DCF, we do not consider this light-curve detection of a stellar rotation harmonic definitive.

3. Radial-velocity Analysis

TOI-216 was monitored with three different high-resolution echelle spectrographs over a time span of 16 months with the goal of obtaining precision radial velocities to further constrain the masses and orbital parameters of the giant planets present in the TOI-216 system. These observations were performed in the context of the Warm gIaNs with tEss (WINE) collaboration, which focuses on the systematic characterization of TESS transiting giant planets with orbital periods longer than ≈ 10 days (e.g., Brahm et al. 2019; Jordán et al. 2020). All radial-velocity measurements of TOI-216 are presented in Table 5.

We obtained 27 spectra with the Fibre-fed, Extended Range, Échelle Spectrograph (FEROS; Kaufer et al. 1999) between 2018 November and 2019 March. FEROS is mounted on the MPG 2.2 m telescope at the ESO La Silla Observatory and has a resolving power of $R \approx 48,000$. Observations were performed with the simultaneous calibration mode for tracing radial-velocity variations produced by environmental changes in the instrument enclosure. The adopted exposure time of 1200 s

Table 3
Light-curve Parameters^a for the TOI-216 System

	q_1		q_2	σ_r		(ppm)	σ_w	(ppm)
TESS	0.29	+0.08 -0.05	0.50	+0.11 -0.10				
	2 minutes	3900	+600 -600	2475	+14 -14			
	20 s	15000	+2000 -2000	5364	+26 -27			
LCOGT i'	0.55	+0.10 -0.10	0.20	+0.07 -0.07	1600	+1970 -1100	1060	+40 -40
Hazelwood g'	0.51	+0.25 -0.15	0.6	+0.2 -0.2	4000	+3000 -3000	2450	+190 -180
El Sauce	0.5	+0.2 -0.2	0.3	+0.2 -0.2	10 ⁴	+4000 -4000	3130	+80 -80
Hazelwood R_c :	0.6	+0.3 -0.4	0.11	+0.18 -0.08				
2019 Nov					9000	+3000 -2000	2100	+200 -200
2020 Feb					10 ⁴	+3000 -3000	1920	+160 -160
LCOGT I :	0.29	+0.07 -0.09	0.49	+0.19 -0.10				
2019 Oct					1400	+1500 -1100	2360	+110 -100
2019 Dec					1200	+1100 -800	1130	+40 -40
2020 Mar					1600	+1400 -1100	990	+50 -50
ASTEP	0.52	+0.18 -0.13	0.4	+0.2 -0.2				
2019 Jun					13000	+2000 -2000	2100	+100 -100
2020 May					3800	+1300 -1100	1270	+50 -50
2020 Jun					11900	+1500 -1500	1360	+70 -70

Note.

^a As a summary statistic, we report the mode and 68.3% confidence interval of the posterior distribution.

yielded spectra with signal-to-noise ratios in the range from 40 to 75. FEROS spectra were processed from raw data with the *ceres* pipeline (Brahm et al. 2017), which delivers precision radial velocities and line bisector span measurements via cross-correlation with a binary mask resembling the spectral properties of a G2-type star. The radial-velocity uncertainties for the FEROS observations of TOI-216 range between 7 and 15 m s⁻¹. We remove two outliers from the FEROS radial-velocity time series at 1503.75 and 1521.57 days. All subsequent results do not include these outliers. We have checked that no results except the inferred jitter for the FEROS data set are sensitive to whether or not the outliers are included.

We observed TOI-216 on 15 different epochs between 2018 December and 2019 October with the High Accuracy Radial velocity Planet Searcher (HARPS; Mayor et al. 2003) mounted on the ESO 3.6 m telescope at the ESO La Silla Observatory, in Chile. We adopted an exposure time of 1800 s for these observations using the high-radial-velocity accuracy mode (HAM; $R \approx 115,000$), which produced spectra with signal-to-noise ratios of ≈ 40 per resolution element. As in the case of FEROS, HARPS data for TOI-216 was processed with the *ceres* pipeline, delivering radial-velocity measurements with typical errors of ≈ 5 m s⁻¹.

TOI-216 was also monitored with the PFS (Crane et al. 2006, 2008, 2010) mounted on the 6.5 m Magellan II Clay Telescope at Las Campanas Observatory (LCO), in Chile. These spectra were obtained on 18 different nights, between 2018 December and 2020 March, using the 0".3 \times 2".5 slit, which delivers a resolving power of $R = 130,000$. Due to its moderate faintness, TOI-216 was observed with the 3 \times 3 binning mode to minimize read-out noise, and an exposure time of 1200 s was adopted to reach a radial-velocity precision of ≈ 2 m s⁻¹. An iodine cell was used in these observations as a reference for the wavelength calibration. The PFS data were processed with a custom IDL pipeline (Butler et al. 1996). Three consecutive 1200 s iodine-free exposures of TOI-216 were obtained to construct a stellar spectral template for

disentangling the iodine spectra from the stellar one for computing the radial velocities.

It is immediately evident that the radial velocities show good agreement with Dawson et al.'s (2019) higher-mass solution, which was fit to the earlier, transit-time-only data set (Figure 3), and with the solution of Kipping et al. (2019) based on transit times from the first six sectors. The bottom panel of Figure 3 shows the radial velocities phased to the outer planet's orbital period. We compute a generalized Lomb–Scargle periodogram (Cumming et al. 1999; Zechmeister & Kürster 2009) in Figures 4 and 5. The x -axis is frequency f in cycles per day. The y -axis is the square root of the power, where we define power as

$$\text{Power}_f = \frac{\sum_i \frac{(v_{i,f} - v_{i,0})^2}{\sigma_i^2} - \sum_i \frac{v_{i,0}^2}{\sigma_i^2}}{2 \sum_i \frac{1}{\sigma_i^2}}, \quad (2)$$

where σ_i is the reported uncertainty (Table 5) and $v_{i,0}$ is the radial-velocity (Table 5) with the error weighted mean $\frac{\sum_i v_i / \sigma_i^2}{\sum_i \frac{1}{\sigma_i^2}}$ for each of the three data sets (PFS, HARPS, and FEROS) subtracted. The sinusoidal function $v_{i,f}$ is

$$v_{i,f} = A \cos[2\pi f(t_i - t_0)] + BA \sin[2\pi f(t_i - t_0)] + C_k, \quad (3)$$

where A and B are computed following Zechmeister & Kürster (2009), k is each of the three data sets, t_0 is the time of the first observed radial velocity, and

$$C_k = - \frac{\sum_i \frac{(A \cos[2\pi f(t_i - t_0)] + BA \sin[2\pi f(t_i - t_0)])}{\sigma_i^2}}{\sum_i \frac{1}{\sigma_i^2}}. \quad (4)$$

We see a peak in the periodogram at planet c 's orbital period (Figure 4, left panel). The noise-free planet c model (overplotted, dashed; a Keplerian signal computed using the parameters of planet c from Table 4 sampled at the observed times in Table 5) shows that many of the other peaks seen in the three periodograms

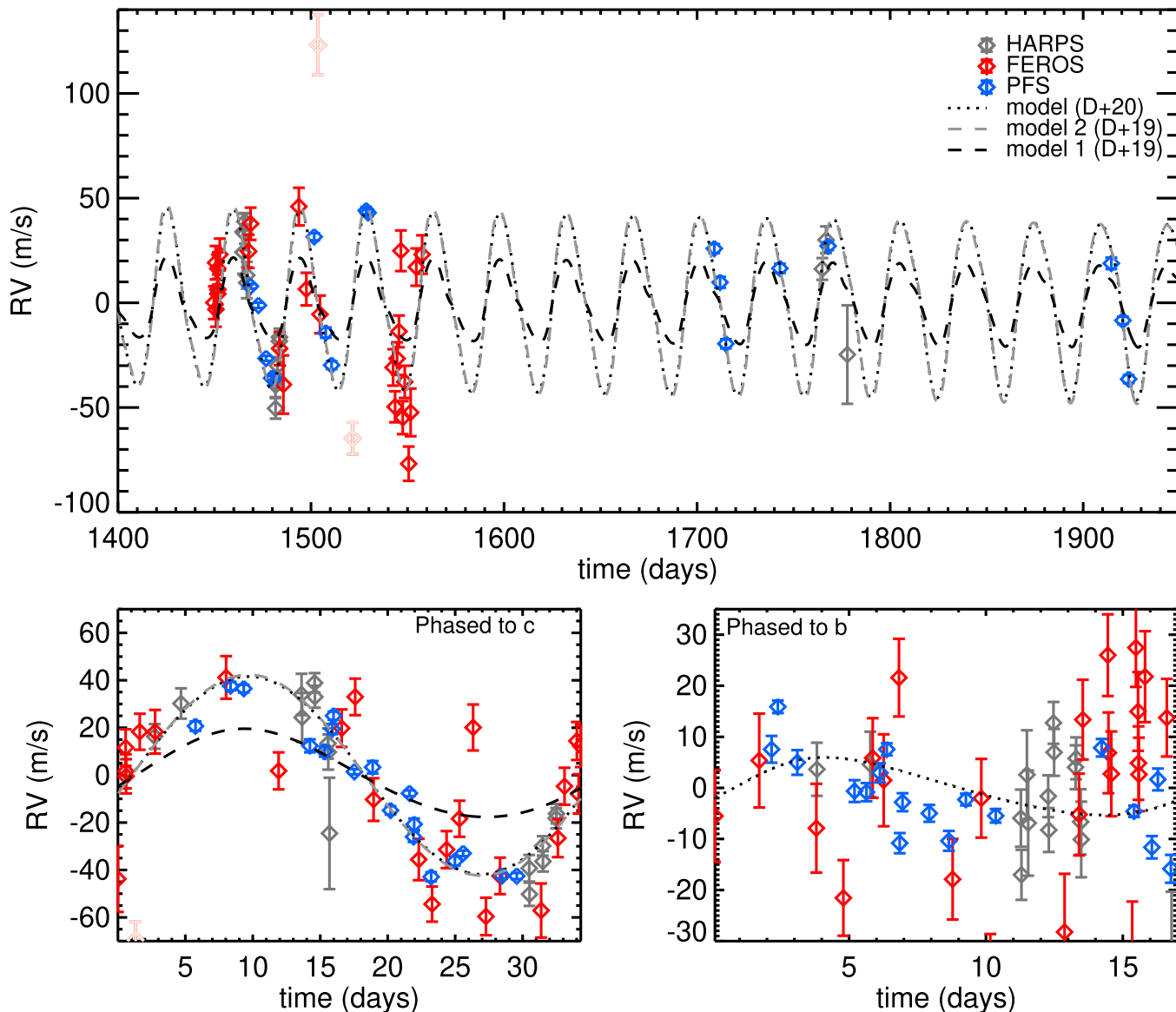


Figure 3. Top: radial-velocity measurements of TOI-216 from HARPS (gray), FEROS (red; outliers in lighter red), and PFS (blue). Best-fit models from this work (Table 4) and from Dawson et al.’s (2019) earlier analysis of transit times only are overplotted. Row 2, left: radial velocities phased to planet c’s orbital period with the same models as row 1 for planet c only (i.e., the radial-velocity variation is only due to planet c) overplotted. Row 2, right: residuals of Table 4 model for planet c only, with the b component of the model overplotted, phased to planet b’s orbital period.

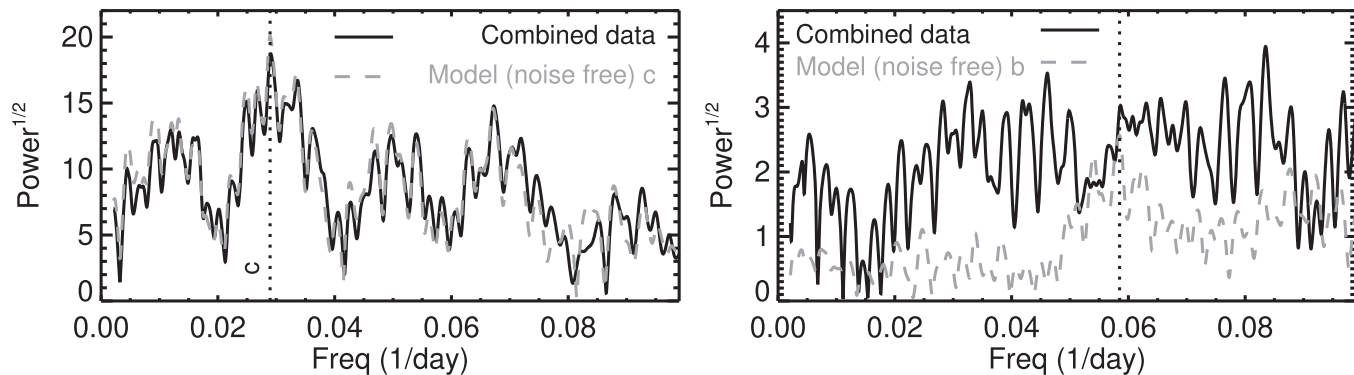


Figure 4. Left: periodograms of the combined radial-velocity data set (black solid), with the periodogram of the noise-free planet c only model (i.e., a Keplerian signal computed using the parameters of planet c from Table 4 sampled at the observed times in Table 5; gray dashed) overplotted. Right: same for the residuals of the planet c only model, with the noise-free planet b only model overplotted (i.e., a Keplerian signal computed using the parameters of planet b from Table 4 sampled at the observed times in Table 5).

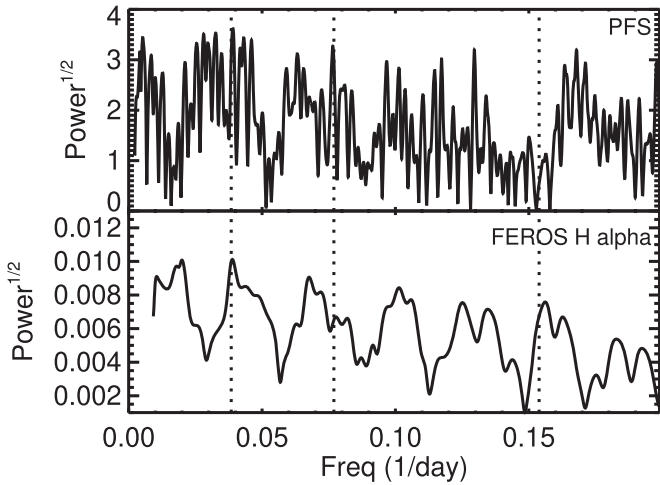


Figure 5. Periodograms of residuals of the best two-planet fit (Table 4) for PSF and H alpha for FEROS. The 6.5, 13, and 26 day periodicities (associated with the periodicity in the light curve; Figure 2) are overlaid as dotted lines.

Table 4

Planet Parameters (Osculating Orbital Elements at Epoch 1325.3279 days) for TOI-216b and TOI-216c Derived from joint TTV/RV fit

Parameter	Value ^a	
$M_*(M_\odot)^b$	0.77	
$R_*(R_\odot)^b$	0.748	
$M_b (M_{\text{Jup}})$	0.059	+0.002 -0.002
P_b	17.0968	+0.0007 -0.0007
e_b	0.160	+0.003 -0.002
ϖ_b (deg.)	291.8	+0.8 -1.0
λ_b (deg)	82.5	+0.2 -0.3
$\Omega_{b,\text{sky}}$ (deg)	0	
$i_{b,\text{sky}}$ (deg)	88.60	+0.03 -0.04
$M_c (M_{\text{Jup}})$	0.56	+0.02 -0.02
P_c	34.5516	+0.0003 -0.0003
e_c	0.0046	+0.0027 -0.0012
ϖ_c (deg.)	190	+30 -50
λ_c (deg)	$27.8^{+1.7}_{-1.5}$	
$\Delta\Omega_{\text{sky}} = \Omega_{c,\text{sky}}$ (deg)	-1	+2 -2
$i_{b,\text{sky}}$ (deg)	89.84	+0.10 -0.08
$2\lambda_c - \lambda_b - \varpi_b$ (deg).	42.5	+0.4 -0.3
$i_{\text{mut}}(\text{deg})^b$	2.0	+1.2 -0.5
Jitter (m/s):		
HARPS	8	+3 -2
FEROS	22	+5 -4
PFS	7.7	+1.7 -1.3

Notes.

^a As a summary statistic we report the median and 68.3% confidence interval of the posterior distribution. An example fit with high precision suitable for numerical integration is given in Table 6.

^b Stellar parameters fixed to the values reported by Dawson et al. (2019): $0.77 \pm 0.03M_\odot$ and $0.748 \pm 0.015R_\odot$. Uncertainties in estimated planetary masses only account for the dynamical fitting, i.e., they *do not* include uncertainties in the star’s mass.

^c 95% confidence interval is 1°–3°9. The 99.7% confidence interval is 1°1–4°3.

are aliases of planet c’s orbital period (i.e., they are caused by the observational time sampling of the planet’s signal). Planet b’s signal is below the noise level (Figure 3, bottom-right panel; Figure 4, right panels). In the PFS data set, including planet b improves the chi-squared from 403 to 328 (for 18 data points and 5 additional parameters); for the HARPS and FEROS data sets, there is no improvement in chi-squared. Given that planet b is barely detected, we cannot rule out other planets in the system with smaller orbital radial-velocity amplitudes.

Systems containing an outer planet in or near a 2:1 mean motion resonance with a less-massive inner planet can be mistaken for a single eccentric planet, because the first-eccentricity harmonic appears at half the planet’s orbital period (e.g., Anglada-Escudé et al. 2010; Kürster et al. 2015). In the case of the system TOI-216, the lack of detection of TOI-216b is not due to this phenomenon because the solution we subtract off for planet c has near-zero eccentricity. However, without prior knowledge that the system contains a resonant pair, if we only had the radial-velocity data sets and the data sets were less noisy (or had more data points), we might be sensitive to planet b’s signal but mistakenly interpret it as planet c’s eccentricity.

The residuals of the two-planet fit (and one-planet fit) show evidence of a signal that we attribute to stellar activity. We examined the periodograms of the residuals of each of three data sets; the bisectors for the HARPS and FEROS data sets; and H alpha for the FEROS data set, computed with the `ceres` pipeline, following Boisse et al. (2009). Periodograms of the PFS residuals and FEROS H alpha are shown in Figure 5. There are no strong peaks in any of the residual or activity indicator periodograms. Some residual data sets exhibit (weak) peaks near the 6.5 day periodicity (HARPS residuals and bisectors; FEROS residuals) identified in the light curve (Section 2), or a multiple of 6.5 days (PFS; FEROS bisectors and H alpha). In Figure 6, we plot the residuals of the two-planet fit with best-fit sinusoids for 6.5, 13, and 26 day periodicities for each data set. Comparing the three data sets, best-fit sinusoids are out of phase with each other. The similarity of the periodicities to those seen in the light curve, the appearance of the 6.5 day periodicity in the HARPS bisectors, the 6.5 and 26 day periodicities in the FEROS H alpha, and the 13 day and 6.5 day periodicities in the FEROS bisectors, and the difference in phase among data sets suggest the weak periodicities do not arise from additional planets. They are possibly caused by stellar variability.

4. Joint Fit and Orbital Architecture

Here we jointly fit the transit light curves (Section 2) and radial-velocity measurements (Section 3) to precisely measure the orbital parameters and masses of both planets. In Section 4.1, we describe our analysis of the transit timing measurements. In Section 4.2, we jointly fit the transit and radial-velocity measurements.

4.1. Transit Timing Variation Analysis

TOI-216b and c exhibit TTVs—plotted in Figure 7—due to the near-resonant effect (e.g., Agol et al. 2005; Lithwick et al. 2012). We have not yet observed a full super-period (which depends on the planets’ proximity to the 2:1 resonance). The amplitude depends on the perturbing planet’s mass and the free eccentricity of the transiting and perturbing planets. We previously found significant free eccentricity, with the exact

Table 5
HARPS, FEROS, and PFS Radial-velocity Measurements of TOI-216

BJD −2450000	RV (m s ^{−1})	σ_{RV} (m s ^{−1})	BIS (m s ^{−1})	σ_{BIS} (m s ^{−1})	Inst.	Note
8449.70722	36690.0	7.8	−16.0	12.0	FEROS	
8450.62181	36709.1	8.0	−12.0	12.0	FEROS	
8450.75019	36686.8	8.3	−35.0	12.0	FEROS	
8451.72708	36706.3	7.7	−21.0	12.0	FEROS	
8451.74212	36696.3	7.2	−44.0	11.0	FEROS	
8451.75750	36694.2	7.2	−25.0	11.0	FEROS	
8452.77587	36713.0	7.6	−48.0	11.0	FEROS	
8464.76381	36754.4	8.7	11.0	11.0	HARPS	
8464.81000	36744.7	10.3	19.0	13.0	HARPS	
8465.73524	36759.3	4.1	9.0	5.0	HARPS	
8465.75656	36753.4	4.6	5.0	6.0	HARPS	
8466.72641	36733.7	6.4	−5.0	8.0	HARPS	
8466.74802	36730.1	7.4	−11.0	10.0	HARPS	
8467.74159	36714.5	7.9	−35.0	12.0	FEROS	
8468.67914	10.49	1.11	PFS	
8468.74406	36727.7	7.7	0.0	12.0	FEROS	
8472.76399	1.38	1.23	PFS	
8476.74101	−23.94	1.18	PFS	
8479.63075	−33.40	1.15	PFS	
8480.71817	−33.50	1.33	PFS	
8481.63918	36681.1	5.6	3.0	7.0	HARPS	
8481.66088	36670.1	4.9	−7.0	6.0	HARPS	
8482.63750	36690.5	4.1	2.0	5.0	HARPS	
8482.65892	36684.0	4.3	−1.0	6.0	HARPS	
8483.63626	36702.2	4.3	−8.0	6.0	HARPS	
8483.65821	36704.1	4.1	11.0	5.0	HARPS	
8483.76291	36668.1	8.0	−1.0	12.0	FEROS	
8485.70826	36650.9	13.9	47.0	19.0	FEROS	
8493.72558	36735.9	9.0	−11.0	13.0	FEROS	
8497.62083	36696.5	7.8	−40.0	12.0	FEROS	
8501.68699	34.11	1.72	PFS	
8503.65356	36813.1	14.3	64.0	19.0	FEROS	Outlier
8504.65888	36684.4	9.0	−61.0	13.0	FEROS	
8507.66569	−11.68	2.42	PFS	
8510.68697	−27.18	1.88	PFS	
8521.56775	36625.2	7.6	5.0	11.0	FEROS	Outlier
8528.60948	46.62	1.76	PFS	
8529.58589	45.56	1.65	PFS	
8542.55798	36659.1	8.7	−44.0	13.0	FEROS	
8543.54347	36640.3	7.4	−6.0	11.0	FEROS	
8544.61674	36663.3	7.8	−26.0	12.0	FEROS	
8545.57452	36676.3	7.6	−3.0	11.0	FEROS	
8546.58251	36714.8	9.7	38.0	14.0	FEROS	
8547.53676	36635.1	7.9	−17.0	12.0	FEROS	
8548.58309	36652.2	7.7	23.0	12.0	FEROS	
8550.61335	36613.1	8.2	−62.0	12.0	FEROS	
8551.62488	36637.6	11.4	−26.0	16.0	FEROS	
8554.56409	36707.0	8.9	−38.0	13.0	FEROS	
8557.56708	36713.0	9.2	−4.0	13.0	FEROS	
8708.90979	28.50	2.14	PFS	
8711.89325	12.38	2.62	PFS	
8714.92414	−16.98	2.14	PFS	
8742.88505	19.06	2.19	PFS	
8764.84159	36736.7	5.2	−1.0	7.0	HARPS	
8766.79176	36750.6	6.4	3.0	8.0	HARPS	
8767.86802	29.71	1.98	PFS	
8777.79725	36695.8	23.5	23.0	31.0	HARPS	
8914.55281	21.41	2.73	PFS	
8920.52884	−5.82	1.77	PFS	
8923.53817	−33.84	1.94	PFS	

Table 6

Example Fit with High-precision Parameters (Osculating Orbital Elements at Epoch 1325.3279 days) for TOI-216b and TOI-216c Derived from Joint TTV/RV Fit

Parameter	Value
$M_*(M_\odot)$	0.77
$M_b (M_{\text{Jup}})$	0.061381
P_b	17.096088
e_b	0.16173
ϖ_b (deg.)	291.14784
λ_b (deg)	82.61190
$\Omega_{b,\text{sky}}$ (deg)	0
$i_{b,\text{sky}}$ (deg)	88.607709
$M_c (M_{\text{Jup}})$	0.58349
P_c	34.55201
e_c	0.0038092
ϖ_c (deg.)	135.86248
λ_c (deg)	25.032
$\Delta\Omega_{\text{sky}} = \Omega_{c,\text{sky}}$ (deg)	-0.19386
$i_{b,\text{sky}}$ (deg)	89.7968

value and partition between planets degenerate with planet mass (Dawson et al. 2019).

We fit the transit times using our N -body integrator TTV model (Dawson et al. 2014). Our model contains five parameters for each planet: the mass M , orbital period P , mean longitude λ , eccentricity e , and argument of periape ω . All orbital elements are osculating orbital elements at the epoch of 1325.3279 days. For each planet, we fix the impact parameter b to the value in Table 2 and set the longitude of ascending node on the sky to $\Omega_{\text{sky}} = 0$. We use the conventional coordinate system where the X - Y plane is the sky plane and the Z -axis points toward the observer. We will explore other possibilities for b and Ω_{sky} in Section 4.2.

We begin by fitting the transit times only. To explore the degeneracy between mass and eccentricity, we use the Levenberg–Marquardt algorithm implemented in IDL `mpfit` (Markwardt 2009) to minimize the χ^2 on a grid of (M_c, e_b) . We first use a data set consisting of all the ground-based data and the TESS Year 1 data. We contour the total χ^2 for 34 transit times and 10 free parameters, i.e., 24 degrees of freedom in Figure 8. Even with the additional transits since Dawson et al. (2019), the fits still suffer from a degeneracy between mass and eccentricity, though the relationship is much tighter. We integrate a random sample of 100 solutions with $\chi^2 < 50$ and find that they all librate in the 2:1 resonance with the resonant angle involving the longitude of periape of the inner planet. Next, we add TESS Year 3 transits from the TESS Extended Mission, which became available while this manuscript was under review. This very extended baseline for the TTVs substantially reduces the degeneracy between mass and eccentricity. We also contour the total χ^2 for these 43 transit times and 10 free parameters, i.e., 33 degrees of freedom, in Figure 8.

A resonant or near-resonant planet’s total eccentricity is the vector sum of its free and forced eccentricity. The forced eccentricity vector is dictated by the resonant dynamics, and the free eccentricity vector oscillates about the tip of the forced vector. Dissipation (e.g., eccentricity damping from the disk) tends to damp the free eccentricity, and other perturbations (e.g., from a third planet) can excite it. We estimate the eccentricity components from simulations as $e_{\text{free}} = (e_{\text{max}} - e_{\text{min}})/2$ and $e_{\text{forced}} = (e_{\text{max}} + e_{\text{min}})/2$. The transit times continue to provide evidence for moderate free eccentricity (Figure 9), but pinning

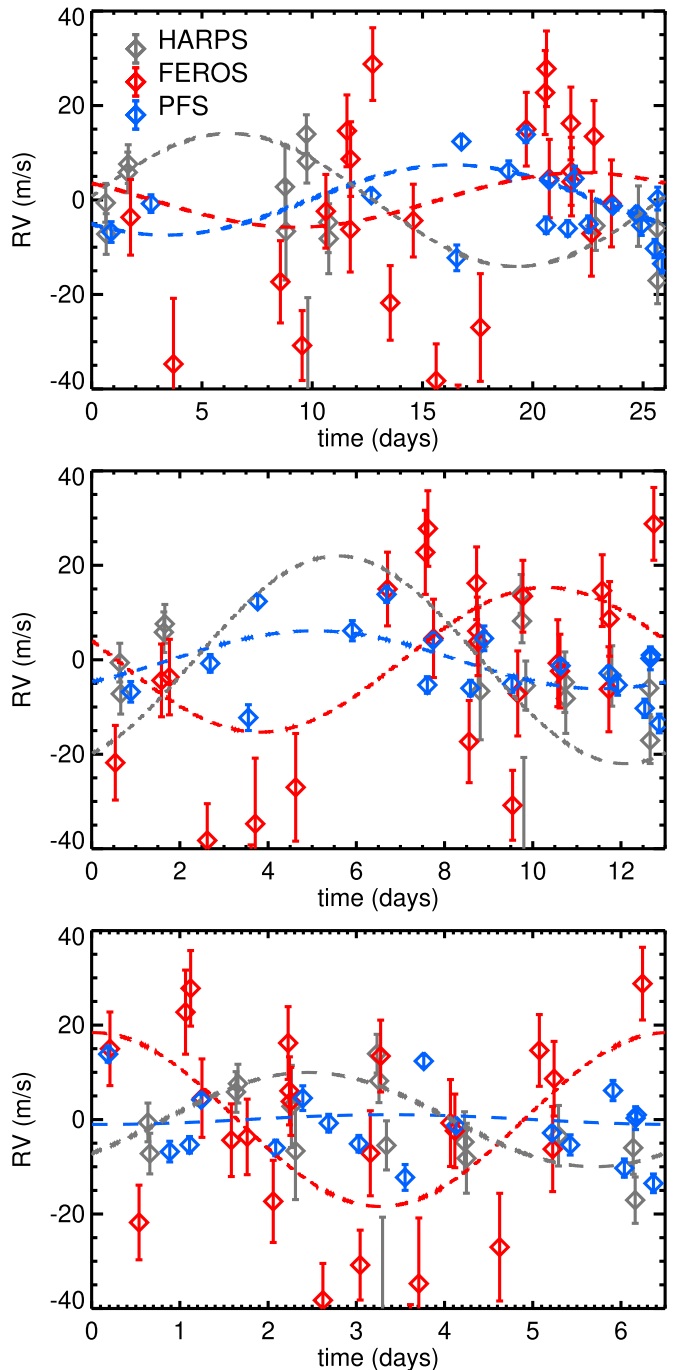


Figure 6. Residuals to the best two-planet fit (Table 4) phased to periodicities of 26 days (top), 13 days (middle), and 6.5 days (bottom). Best-fit sinusoids for these periodicities are overplotted as dashed lines. Comparing the three data sets, the best-fit sinusoids are out of phase with each other, indicating that these signals are unlikely to arise from additional planets.

down the outer planet’s mass with a joint radial-velocity fit will allow for a tighter constraint.

4.2. Joint Transit and Radial-velocity Fit

We perform a joint N -body fit to the transit times and radial velocities, imposing two additional constraints. One constraint is the transit exclusion intervals reported in Dawson et al. (2019). The other is the light-curve joint posterior of stellar density ρ_{circ} versus impact parameter b (Table 2; Equation (1))

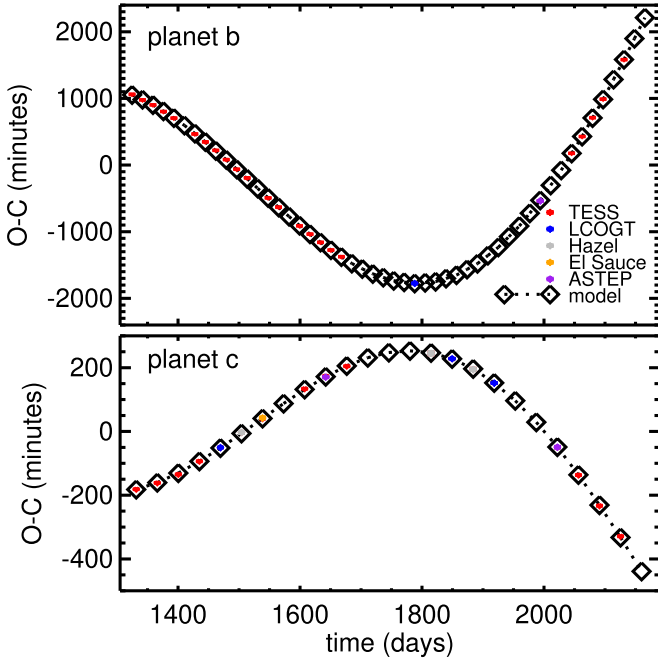


Figure 7. Observed midtransit times (diamonds) with subtracted linear ephemeris for TOI-216b (top) and TOI-216c (bottom), with the best-fit model overlotted (diamonds, dotted line).

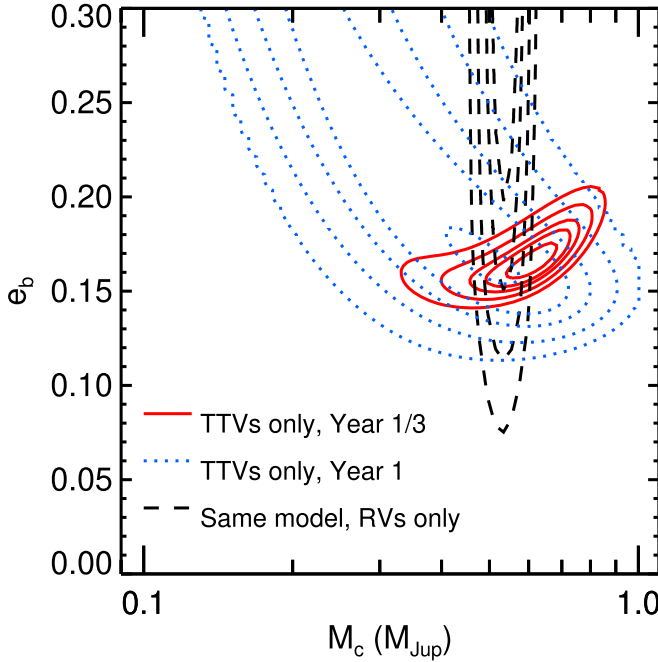


Figure 8. Contours of χ^2 for the fit to transit times only. With ground-based transits and Year 1 of TESS data (blue dotted line), fits to the transit times only result in degeneracy between the inner planet’s (osculating) eccentricity and the outer planet’s mass. The levels are $\chi^2 = 42, 47, 52, 62,$ and $77,$ and the best-fit solutions occupy the innermost contour. The black contours show the χ^2 for these same solutions compared to the RV measurements, with a radial-velocity offset for each instrument as the only free parameter. The levels are $\chi^2 = 540, 560, 600,$ and 650 and the best-fit solutions occupy the innermost contour. The RV measurements break the degeneracy between mass and eccentricity. The addition of Year 3 TESS Extended Mission data (through sector 30; red solid) reduces the degeneracy between mass and eccentricity and shows good agreement with the radial-velocity data. The levels are $\chi^2 = 65, 70, 75, 85,$ and $100,$ and the best-fit solutions occupy the innermost contour.

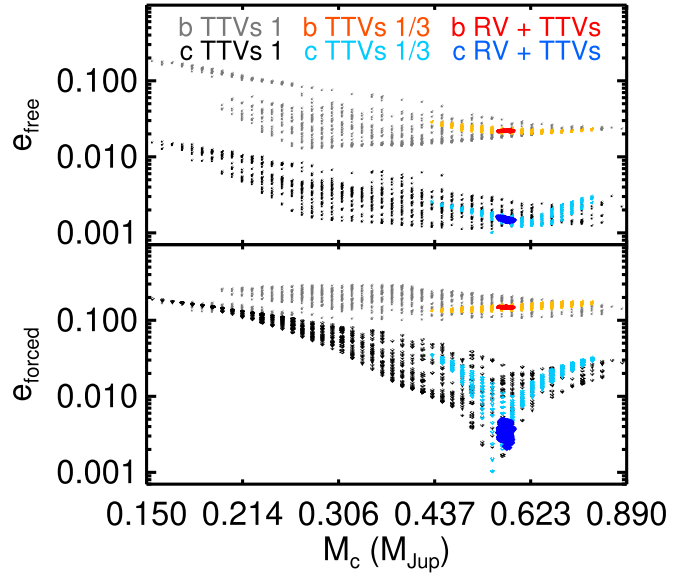


Figure 9. Long-term (10^6 days) behavior of solutions with $\chi^2 < 60$ (TTV-only fits with ground-based transits and Year 1 of TESS data, gray and black, which have discrete values because they are performed on a grid); $\chi^2 < 80$ (TTV-only fits with addition of Year 3 TESS Extended Mission data, orange and light blue); and from the MCMC posterior for the joint RV-TTV fit (red and blue, Table 4). Row 1: e_{free} (approximated as $(e_{\text{max}} - e_{\text{min}})/2$); Row 2: e_{forced} (approximated as $(e_{\text{max}} + e_{\text{min}})/2$).

combined with the ρ_* posterior from Dawson et al. (2019). Following Dawson & Johnson (2012), we convert the ρ_{circ} versus b to a g versus b posterior according to $g = (\rho_{\text{circ}}/\rho_*)^{1/3}$. We use the g versus b posterior to add a term to the likelihood based on e and ω using $g = (1 + e \sin \omega)/(1 - e^2)^{1/2}$. We compute the sky-plane inclination for the dynamical model from b according to $\sin i_{\text{sky}} a/R_* = (1 + e \sin \omega)/(1 - e^2)$.

Following Dawson et al. (2014), we derive posteriors for the parameters using MCMC with the Metropolis–Hastings algorithm. Instead of including the orbital period and mean longitude at epoch 1325.3279 days as parameters in the MCMC, we optimize them at each jump (i.e., each MCMC step) using the Levenberg–Marquardt algorithm (i.e., optimizing the dynamical model). We also optimize the radial-velocity offset for each instrument at each jump. We fit for a radial-velocity jitter term for each of the three instruments; even though we identified possible periodicities in Figure 5, none are strong enough to justify to explicitly modeling (e.g., with false-alarm probabilities of 0.2, 0.002, and 0.02 for the highest peak in the periodogram for PFS, FEROS, and HARPS, respectively; Cumming 2004). We visually inspect each parameter for convergence. We know there is a mutual inclination perpendicular to the sky plane because the inner planet exhibits grazing transits and the outer planet does not. To also allow for a mutual inclination parallel to the sky plane, we fit for $\Delta\Omega_{\text{sky}}$, the difference in longitude of ascending node.

Following Dawson et al. (2019), we perform two fits with different priors to assess the sensitivity to these priors. The first solution (Table 4) imposes uniform priors on eccentricities and log-uniform priors on mass (i.e., priors that are uniform in log space). The second imposes uniform priors on mass and log-uniform priors on eccentricity. All other fitted parameters (orbital period, mean longitude, argument of periaapse, radial-velocity jitters, difference in longitude of ascending node) have

uniform priors. With the data set in Dawson et al. (2019), the results were very sensitive to the priors; with the new data set that includes radial velocities and an expanded TTV baseline, the results with different priors are nearly indistinguishable. In both cases, we impose the 3σ limits on change in transit duration derived in Section 2. We measure a small but significant mutual inclination of $1^\circ 2' - 3^\circ 9'$ (95% confidence interval). An example fit with high precision suitable for numerical integration is given in Table 6.

To ensure that our results are robust and that the parameter space has been thoroughly explored by the fitting algorithm (particularly the degeneracy between eccentricity and mass), we carry out a fit using a different N -body code and fitting algorithm. We use the Python Tool for Transit Variations (PYTTV; Korth 2020) to fit the transit times (Table 2), radial velocities (Table 5), and the stellar parameters reported in Dawson (2020). The parameter estimation is carried out by a joint N -body fit using Rebound with the IAS15 integrator (Rein & Liu 2012; Rein & Spiegel 2015) and Reboundx (Tamayo et al. 2020), to model all of the observables without approximations. Within the simulation, carried out in barycentric coordinates, a common coordinate system was chosen where the x - y plane is the plane of sky. The x -axis points to the east, the y -axis points to the north, and the z -axis points to the observer. Ω is measured from east to north, and ω is measured from the plane of sky. For the parameter estimation with PYTTV, the gravitational forces between the planets and the influence of general relativity (GR) were considered, in case the influence of GR is significant enough to be visible in the TTVs; for this system, general relativistic precession does not significantly affect the TTVs. The parameter estimation is initialized using Rayleigh priors on eccentricities (Van Eylen et al. 2019) and uniform priors on log values for the planetary masses. The estimation of physical quantities from the TTV signal is done in two steps. First, the posterior mode is found using the differential evolution algorithm implemented in PyTransit (Parviainen 2015). The optimization is carried out varying the planetary masses, orbital periods, inclinations, eccentricities and arguments of periastron. The eccentricity and argument of periastron are mapped from sampling parameters $\sqrt{e} \cos \omega$ and $\sqrt{e} \sin \omega$. The longitudes of the ascending nodes are fixed for both planets. After the posterior mode is found, a sample from the posterior is obtained using the affine-invariant MCMC ensemble sampler emcee (Foreman-Mackey et al. 2013). The parameters and uncertainties are consistent with those reported in Table 4.

4.3. Dynamics and Origin

We randomly draw 1000 solutions from the posterior for longer integrations of 10^6 days using `mercury6` (Chambers et al. 1996). We compute the libration amplitudes for the 2:1 resonant angle $2\lambda_c - \lambda_b - \varpi_b$, where the longitude of periastron $\varpi_b = \omega_b + \Omega_b$. We can now definitively determine that the system is librating in resonance. The libration amplitude is well constrained to 60_{-2}^{+2} deg. The very small uncertainty in libration amplitude leads us to believe that its moderate value is real, not an artifact of imperfect characterization (e.g., Millholland et al. 2018). Figure 10 shows a trajectory demonstrating libration about a fixed point. In our solutions, the other 2:1 resonant angle $2\lambda_c - \lambda_b - \varpi_c$ always circulates. However, the outer planet’s eccentricity and longitude of periastron are poorly constrained, so it is possible that solutions where this angle librates are also consistent with the data. The inner planet has a forced eccentricity (Figure 9) of $0.146_{-0.003}^{+0.003}$ and a modest but significant free eccentricity of $0.0222_{-0.0003}^{+0.0005}$. The outer

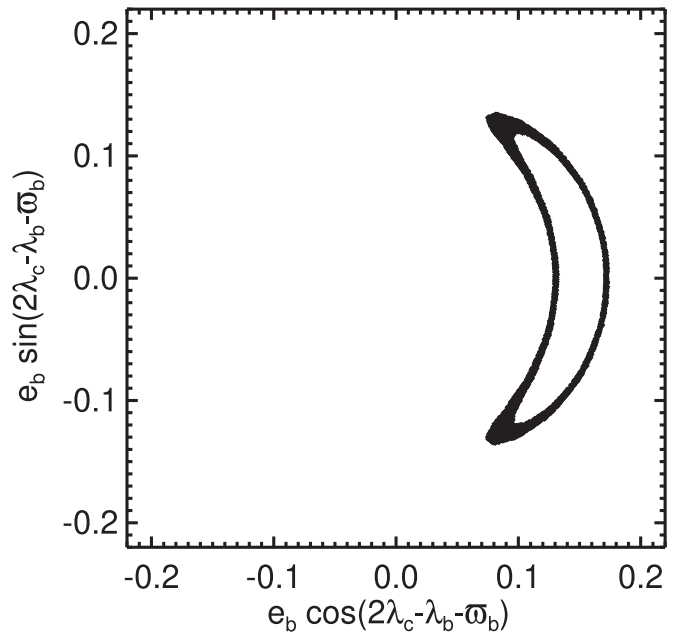


Figure 10. Example trajectory for TOI-216 solution. The trajectory does not pass through the origin, indicating libration about a fixed point. The offset from the origin is the forced eccentricity.

planet has very small forced and free eccentricities of $0.0048_{-0.0013}^{+0.0028}$ and $0.00162_{-0.00010}^{+0.00011}$ respectively. In our integrated solutions, we find that the timescale for the biggest variations in both planets’ semi-major axes and the inner planet’s eccentricity is the resonant libration timescale (approximately 5 years), and the outer planet’s eccentricity varies on apsidal alignment timescale (approximately 25 years). This system falls into the regime of resonant TTVs (e.g., Nesvorný & Vokrouhlický 2016)—rather than the more commonly characterized near-resonant TTVs (e.g., Lithwick et al. 2012)—and we expect the TTVs to oscillate on the libration timescale, which has not yet been fully covered by the observational baseline (Figure 7). We integrate a random subset of 200 solutions for 1 Myr and find that all are stable.

One possible scenario for establishing the resonance is convergent migration of planet c preceded or followed by perturbations of planet b by another body (Figure 11). We show example simulations that apply a migration force using the user-defined force feature of `mercury6` (as described in Wolff et al. 2012); the simulations are done in 3D with initial inclinations set to the present-day values. Planet c migrates a short distance (0.8% of its initial semimajor axis) toward planet b and captures b into resonance. In the first example (top), planet b starts with a modestly eccentric (bottom) orbit ($e = 0.0798$). In the second example, planet b starts with a lower eccentricity ($e = 0.02$) and is captured into resonance with a tight libration amplitude. At about 80,000 yr, planet b’s orbit is disturbed, which we approximate as an instantaneous change in the magnitude and direction of its eccentricity vector. The first history results in large-amplitude libration of the resonant angle involving ϖ_c and the second in circulation; because we are not confident that only circulating resonant angles are compatible with the data, we cannot use this distinction to favor one history over the other.

These example dynamical histories are compatible with in situ formation but are potentially compatible with long-distance migration as well. In the in situ formation scenario, three or more planets form in situ, and planet c migrates a tiny distance toward b. A third planet jostles b—exciting its eccentricity and mutual

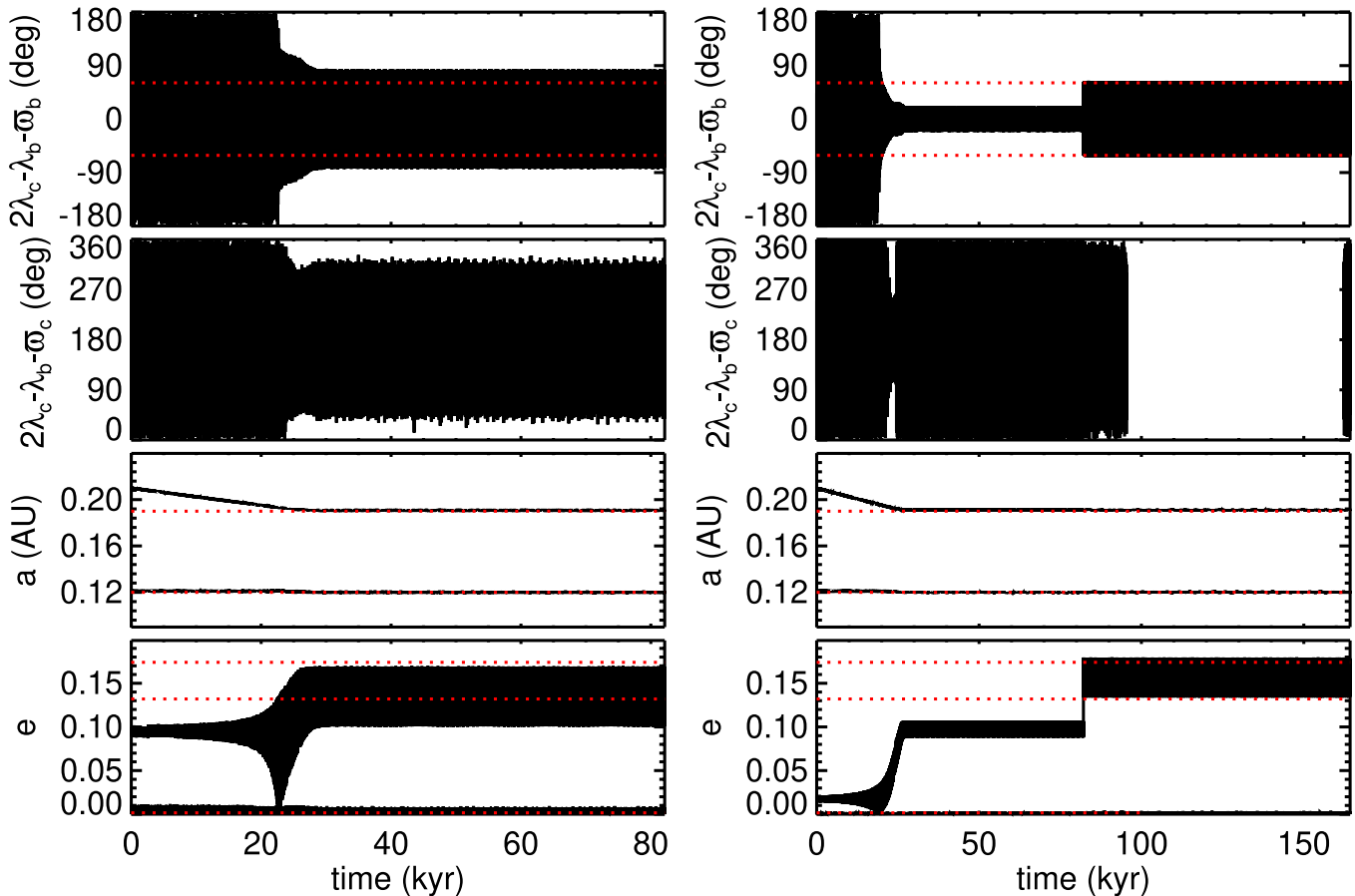


Figure 11. Examples of resonance capture through short-distance convergent migration of planet c. Rows 1–2: resonant angle, row 3: semimajor axis of planet c (top black line) and planet b (bottom black line), row 4: eccentricity of planet b (top black line) and planet b (bottom black line). Values from simulations with the present-day observed orbits (i.e., range of oscillation) are marked with a dotted red line.

inclination—before or after c’s migration. In the long-distance migration scenario, the disturbing third planet could have migrated earlier. As future work, orbital dynamics simulations could place limits on the properties of this possible third planet. Although we have invoked a third planet in the example scenarios, we have not ruled out the possibility that planet b itself disturbed planet c, in a process separate from migration.

Another hypothesis for the mutual inclination is that it was excited when the planets passed through the 4:2 inclination resonance during migration (Thommes & Lissauer 2003). Precession from the protoplanetary disk can separate the 4:2 inclination resonances from the 2:1 eccentricity resonance. Figure 12 shows a proof-of-concept simulation where the potential of the protoplanetary disk is approximated as a J_2 oblateness term for the stellar potential. A small but significant mutual inclination is excited.

We place planet b and c on a mass–radius plot of warm exoplanets in Figure 13. TOI-216c has a typical radius for its mass; its bulk density is $0.885^{+0.014}_{-0.013} \text{ g cm}^{-3}$. TOI-216b likely also has a typical radius for its mass, but because of its grazing transit (Section 2) and the resulting degeneracy with impact parameter, we cannot rule out a large radius that would result in a low density for its mass compared to similar mass planets. Its poorly constrained bulk density is $0.17^{+0.18}_{-0.10} \text{ g cm}^{-3}$.

5. Conclusion

TOI-216b and c are now a very precisely characterized (with the exception of planet b’s radius) pair of warm, large

exoplanets. Radial-velocity measurements using HARPS, FEROS, and PFS broke a degeneracy between mass and eccentricity in the TTV-only fits that was particularly severe before the TESS Extended Mission observations, and an expanded TTV baseline from TESS and an ongoing ground-based transit observing campaign increased the precision of the fits. We can now better assess the consistency of its properties with different theories for the formation and evolution of giant planets orbiting close to their stars.

We now know that TOI-216c is a warm Jupiter (0.54 ± 0.02 Jupiter masses) with a mass and radius typical of other 10–200 days giant planets (Figure 13). TOI-216b has a mass similar to Neptune’s ($18.4 \pm 0.6 M_{\oplus}$). Its radius is not well constrained due to its grazing transits; its radius may very well be typical for its mass (Figure 13). Given the large uncertainty in planet b’s radius, no inflation mechanisms or scenarios requiring formation beyond the ice line (e.g., Lee & Chiang 2016) are required to explain either planet’s radius.

Furthermore, we know now that TOI-216b and c are not just near but librating in 2:1 resonance. The argument involving the longitude of periastron of TOI-216b librates with an amplitude of 60^{+2}_{-2} deg . TOI-216b has a small but significant free eccentricity $0.0222^{+0.0005}_{-0.0003}$. The mutual inclination with respect to TOI-216c is between $1^{\circ}2$ and $3^{\circ}9$ (95% confidence interval). The libration amplitude, free eccentricity, and mutual inclination imply a disturbance of TOI-216b before or after resonance capture, perhaps by an undetected third planet. The orbital properties can be consistent either with in situ formation, with

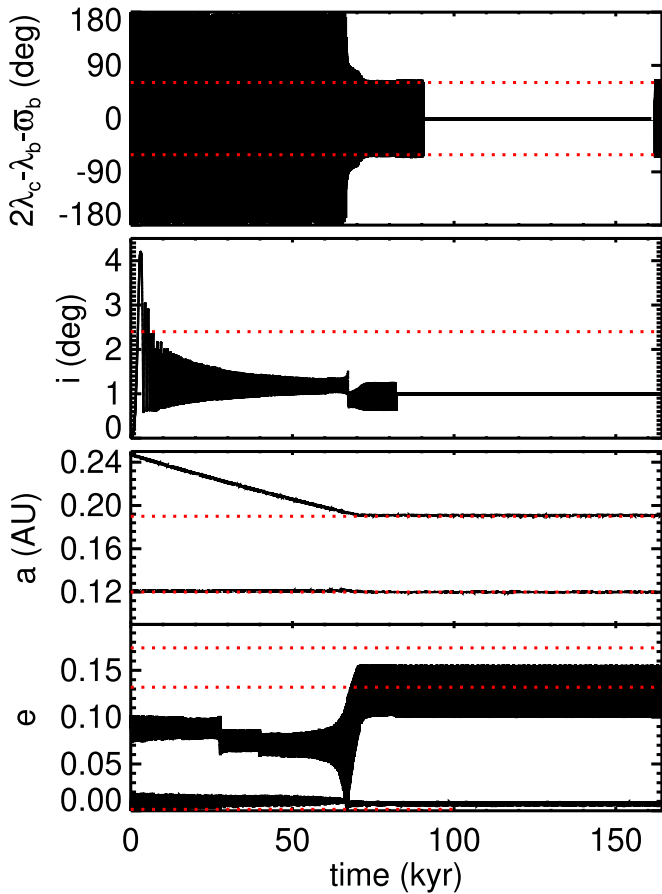


Figure 12. Examples of excitation of a mutual inclination during short-distance convergent migration of planet c. Row 1: eccentricity resonant angle, row 2: mutual inclination, row 3: semimajor axis of planet c (top black line) and planet b (bottom black line), row 4: eccentricity of planet b (top black line) and planet c (bottom black line). Values from simulations with the present-day observed orbits (i.e., range of oscillation) are marked with a dotted red line.

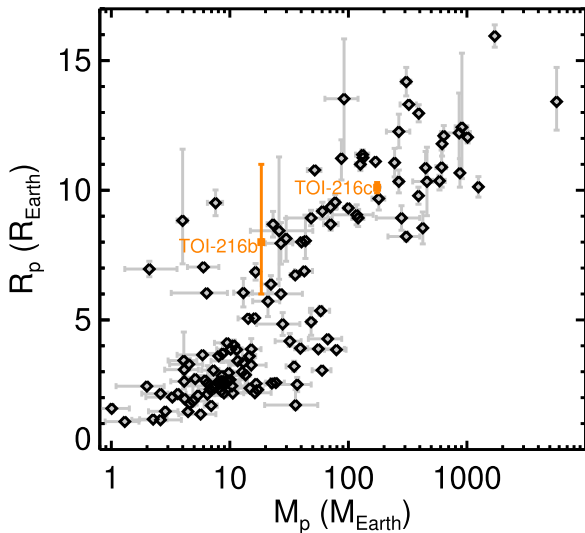


Figure 13. Warm (10–200 day orbital period) planets with both mass and radius measurements (exoplanet.eu; Schneider et al. 2011), including TOI-216 (orange).

resonance capture through a very-short-distance migration, or long-distance migration. Future origin scenarios must match these precisely constrained properties. Future atmospheric characterization by the James Webb Space Telescope (JWST)

may help distinguish between these origin scenarios. If the planet formed outside the water snow line, we expect its C/O ratio to be significantly smaller than that of its host star; in situ formation, on the other hand, would imply C/O ratios closer to the star (Espinoza et al. 2017). Simulations performed with PandExo (Batalha et al. 2017) show that water features in the spectra that constrain the C/O ratio may be detectable for TOI-216c with the JWST Near Infrared Imager and Slitless Spectrograph, even beneath a moderate cloud layer.

This system will benefit from continued long-term radial-velocity and transit monitoring. Long-term radial-velocity monitoring could reveal the presence of additional planets in the system, though stellar activity poses a challenge for detecting low-amplitude signals. Observations by the TESS Extended Mission are continuing and will further increase the baseline of observations. The new TESS observations may allow us to better constrain the change in impact parameter tentatively detected here for TOI-216b, allowing for tighter constraints on the mutual inclination.

We thank the TESS mission team and follow-up working group for the valuable data set. We acknowledge the use of public TESS Alert data from pipelines at the TESS Science Office and at the TESS Science Processing Operations Center. This paper includes data collected by the TESS mission, which are publicly available from the Mikulski Archive for Space Telescopes (MAST). Resources supporting this work were provided by the NASA High-End Computing (HEC) Program through the NASA Advanced Supercomputing (NAS) Division at Ames Research Center for the production of the SPOC data products.

This research has made use of the Exoplanet Follow-up Observation Program website, which is operated by the California Institute of Technology, under contract with the National Aeronautics and Space Administration under the Exoplanet Exploration Program. This work has made use of observations from the Las Cumbres Observatory network. This work has made use of data from the European Space Agency (ESA) mission Gaia (<https://www.cosmos.esa.int/gaia>), processed by the Gaia Data Processing and Analysis Consortium (DPAC, <https://www.cosmos.esa.int/web/gaia/dpac/consortium>). Funding for the DPAC has been provided by national institutions, in particular the institutions participating in the Gaia Multilateral Agreement. We acknowledge support for ASTEP from the French and Italian Polar Agencies, IPEV and PNRA, and from Université Côte d’Azur under Idex UCAJEDI (ANR-15-IDEX-01). This paper includes data gathered with the 6.5 m Magellan Telescopes located at Las Campanas Observatory, Chile.

R.I.D. and J.D. gratefully acknowledge support by NASA XRP NNX16AB50G, NASA XRP 80NSSC18K0355, NASA TESS GO 80NSSC18K1695, and the Alfred P. Sloan Foundation’s Sloan Research Fellowship. The Center for Exoplanets and Habitable Worlds is supported by the Pennsylvania State University, the Eberly College of Science, and the Pennsylvania Space Grant Consortium. J.D. gratefully acknowledges support and hospitality from the pre-doctoral program at the Center for Computational Astrophysics, Flatiron Institute. Research at the Flatiron Institute is supported by the Simons Foundation. This research made use of computing facilities from Penn State’s Institute for CyberScience Advanced CyberInfrastructure.








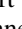
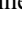


We thank Caleb Cañas and David Nesvorný for helpful comments and discussions. We thank the referee for a helpful report.

R.B. acknowledges support from FONDECYT Project 11200751 and from CORFO project No. 14ENI2-26865. A. J., R.B., and M.H. acknowledge support from project IC120009 “Millennium Institute of Astrophysics (MAS)” of the Millennium Science Initiative, Chilean Ministry of Economy. A.J. acknowledges additional support from FONDECYT project 1171208. This research received funding from the European Research Council (ERC) under the European Union’s Horizon 2020 research and innovation program (grant agreement No. 803193/BEBOP), and from the Science and Technology Facilities Council (STFC; grant No. ST/S00193X/1). J. Korth acknowledges support by DFG grants PA525/19-1 within the DFG Schwerpunkt SPP 1992, Exploring the Diversity of Extrasolar Planets. Part of this research was carried out at the Jet Propulsion Laboratory, California Institute of Technology, under a contract with the National Aeronautics and Space Administration (NASA).

Software: mpfit (Markwardt 2009), TAP (Gazak et al. 2012), Tapir (Jensen 2013), TESS pipeline (Jenkins et al. 2016; Twicken et al. 2018; Li et al. 2019), AstroImageJ (Collins et al. 2017), exoplanet (Foreman-Mackey et al. 2019), astropy (Astropy Collaboration et al. 2013, 2018), celerite (Foreman-Mackey et al. 2017; Foreman-Mackey 2018), starry (Luger et al. 2019), pymc3 (Salvatier et al. 2016), theano (Theano Development Team 2016), ceres (Brahm et al. 2017), PyTTV, PyTransit (Parviainen 2015), emcee (Foreman-Mackey et al. 2013), eleanor (Feinstein et al. 2019).

ORCID iDs

Rebekah I. Dawson  <https://orcid.org/0000-0001-9677-1296>
 Chelsea X. Huang  <https://orcid.org/0000-0003-0918-7484>
 Rafael Brahm  <https://orcid.org/0000-0002-9158-7315>
 Karen A. Collins  <https://orcid.org/0000-0001-6588-9574>
 Melissa J. Hobson  <https://orcid.org/0000-0002-5945-7975>
 Jiayin Dong  <https://orcid.org/0000-0002-3610-6953>
 Trifon Trifonov  <https://orcid.org/0000-0002-0236-775X>
 R. Paul Butler  <https://orcid.org/0000-0003-1305-3761>
 Mauro Barbieri  <https://orcid.org/0000-0001-8362-3462>
 Kevin I. Collins  <https://orcid.org/0000-0003-2781-3207>
 Dennis M. Conti  <https://orcid.org/0000-0003-2239-0567>
 Jeffrey D. Crane  <https://orcid.org/0000-0002-5226-787X>
 Nicolas Crouzet  <https://orcid.org/0000-0001-7866-8738>
 Néstor Espinoza  <https://orcid.org/0000-0001-9513-1449>
 Tianjun Gan  <https://orcid.org/0000-0002-4503-9705>
 Tristan Guillot  <https://orcid.org/0000-0002-7188-8428>
 Thomas Henning  <https://orcid.org/0000-0002-1493-300X>
 Eric L. N. Jensen  <https://orcid.org/0000-0002-4625-7333>
 Djamel Mékarnia  <https://orcid.org/0000-0001-5000-7292>
 Gordon Myers  <https://orcid.org/0000-0002-9810-0506>
 Paula Sarkis  <https://orcid.org/0000-0001-8128-3126>
 Stephen Shectman  <https://orcid.org/0000-0002-8681-6136>
 François-Xavier Schmider  <https://orcid.org/0000-0003-3914-3546>
 Avi Shporer  <https://orcid.org/0000-0002-1836-3120>
 Chris Stockdale  <https://orcid.org/0000-0003-2163-1437>
 Amaury H. M. J. Triaud  <https://orcid.org/0000-0002-5510-8751>
 Carl Ziegler  <https://orcid.org/0000-0002-0619-7639>

G. Ricker  <https://orcid.org/0000-0003-2058-6662>
 R. Vanderspek  <https://orcid.org/0000-0001-6763-6562>
 David W. Latham  <https://orcid.org/0000-0001-9911-7388>
 J. Winn  <https://orcid.org/0000-0002-4265-047X>
 Jon M. Jenkins  <https://orcid.org/0000-0002-4715-9460>
 L. G. Bouma  <https://orcid.org/0000-0002-0514-5538>
 Jennifer A. Burt  <https://orcid.org/0000-0002-0040-6815>
 David Charbonneau  <https://orcid.org/0000-0002-9003-484X>
 Brian McLean  <https://orcid.org/0000-0002-8058-643X>
 Mark E. Rose  <https://orcid.org/0000-0003-4724-745X>
 Andrew Vanderburg  <https://orcid.org/0000-0001-7246-5438>

References

- Agol, E., Steffen, J., Sari, R., & Clarkson, W. 2005, *MNRAS*, 359, 567
 Anderson, K. R., Lai, D., & Pu, B. 2020, *MNRAS*, 491, 1369
 Anglada-Escudé, G., López-Morales, M., & Chambers, J. E. 2010, *ApJ*, 709, 168
 Astropy Collaboration, Price-Whelan, A. M., Sipőcz, B. M., et al. 2018, *AJ*, 156, 123
 Astropy Collaboration, Robitaille, T. P., Tollerud, E. J., et al. 2013, *A&A*, 558, A33
 Batalha, N. E., Mandell, A., Pontoppidan, K., et al. 2017, *PASP*, 129, 064501
 Boisse, I., Moutou, C., Vidal-Madjar, A., et al. 2009, *A&A*, 495, 959
 Brahm, R., Espinoza, N., Jordán, A., et al. 2019, *AJ*, 158, 45
 Brahm, R., Jordán, A., & Espinoza, N. 2017, *PASP*, 129, 034002
 Brown, T. M., Baliber, N., Bianco, F. B., et al. 2013, *PASP*, 125, 1031
 Butler, R. P., Marcy, G. W., Williams, E., et al. 1996, *PASP*, 108, 500
 Canto Martins, B. L., Gomes, R. L., Messias, Y. S., et al. 2020, *ApJS*, 250, 20
 Carter, J. A., & Winn, J. N. 2009, *ApJ*, 704, 51
 Chambers, J. E., Wetherill, G. W., & Boss, A. P. 1996, *Icar*, 119, 261
 Choksi, N., & Chiang, E. 2020, *MNRAS*, in press
 Collins, K. A., Kielkopf, J. F., Stassun, K. G., & Hessman, F. V. 2017, *AJ*, 153, 77
 Crane, J. D., Shectman, S. A., & Butler, R. P. 2006, *Proc. SPIE*, 6269, 626931
 Crane, J. D., Shectman, S. A., Butler, R. P., et al. 2010, *Proc. SPIE*, 7735, 773553
 Crane, J. D., Shectman, S. A., Butler, R. P., Thompson, I. B., & Burley, G. S. 2008, *Proc. SPIE*, 7014, 701479
 Cumming, A. 2004, *MNRAS*, 354, 1165
 Cumming, A., Marcy, G. W., & Butler, R. P. 1999, *ApJ*, 526, 890
 Dawson, R. I. 2020, *AJ*, 159, 223
 Dawson, R. I., Huang, C. X., Lissauer, J. J., et al. 2019, *AJ*, 158, 65
 Dawson, R. I., & Johnson, J. A. 2012, *ApJ*, 756, 122
 Dawson, R. I., & Johnson, J. A. 2018, *ARA&A*, 56, 175
 Dawson, R. I., Johnson, J. A., Fabrycky, D. C., et al. 2014, *ApJ*, 791, 89
 Deck, K. M., & Agol, E. 2015, *ApJ*, 802, 116
 Dong, R., & Dawson, R. 2016, *ApJ*, 825, 77
 Edelson, R. A., & Krolik, J. H. 1988, *ApJ*, 333, 646
 Espinoza, N., Fortney, J. J., Miguel, Y., Thorngren, D., & Murray-Clay, R. 2017, *ApJ*, 838, L9
 Feinstein, A. D., Montet, B. T., Foreman-Mackey, D., et al. 2019, *PASP*, 131, 094502
 Foreman-Mackey, D. 2018, *RNAAS*, 2, 31
 Foreman-Mackey, D., Agol, E., Ambikasaran, S., & Angus, R. 2017, *AJ*, 154, 220
 Foreman-Mackey, D., Czekala, I., Luger, R., et al. 2019, *dfm/exoplanet-exoplanet v0.2.1*, Zenodo, doi:10.5281/zenodo.3462740
 Foreman-Mackey, D., Hogg, D. W., Lang, D., & Goodman, J. 2013, *PASP*, 125, 306
 Frelikh, R., Jang, H., Murray-Clay, R. A., & Petrovich, C. 2019, *ApJ*, 884, L47
 Gazak, J. Z., Johnson, J. A., Tonry, J., et al. 2012, *AdAst*, 2012, 697967
 Huang, C., Wu, Y., & Triaud, A. H. M. J. 2016, *ApJ*, 825, 98
 Jenkins, J. M., Caldwell, D. A., & Borucki, W. J. 2002, *ApJ*, 564, 495
 Jenkins, J. M., Caldwell, D. A., Chandrasekaran, H., et al. 2010, *ApJ*, 713, L87
 Jenkins, J. M., Twicken, J. D., McCauliff, S., et al. 2016, *Proc. SPIE*, 9913, 99133E
 Jensen, E. 2013, Tapir: A Web Interface for Transit/Eclipse Observability, Astrophysics Source Code Library, ascl:1306.007
 Jordán, A., Brahm, R., Espinoza, N., et al. 2020, *AJ*, 159, 145

- Kaufer, A., Stahl, O., Tubbesing, S., et al. 1999, *Msngr*, **95**, 8
- Kipping, D., Nesvorný, D., Hartman, J., et al. 2019, *MNRAS*, **486**, 4980
- Kipping, D. M. 2013, *MNRAS*, **435**, 2152
- Korth, J. 2020, PhD thesis, Univ. Cologne, <https://kups.uni-koeln.de/11289/>
- Kürster, M., Trifonov, T., Reffert, S., Kostogryz, N. M., & Rodler, F. 2015, *A&A*, **577**, A103
- Lee, E. J., & Chiang, E. 2016, *ApJ*, **817**, 90
- Lee, M. H., & Peale, S. J. 2002, *ApJ*, **567**, 596
- Li, J., Tenenbaum, P., Twicken, J. D., et al. 2019, *PASP*, **131**, 024506
- Lithwick, Y., & Naoz, S. 2011, *ApJ*, **742**, 94
- Lithwick, Y., Xie, J., & Wu, Y. 2012, *ApJ*, **761**, 122
- Luger, R., Agol, E., Foreman-Mackey, D., et al. 2019, *AJ*, **157**, 64
- MacDonald, M. G., & Dawson, R. I. 2018, *AJ*, **156**, 228
- Mandel, K., & Agol, E. 2002, *ApJ*, **580**, L171
- Markwardt, C. B. 2009, in ASP Conf. Ser. 411, *Astronomical Data Analysis Software and Systems XVIII*, ed. D. A. Bohlender, D. Durand, & P. Dowler (San Francisco, CA: ASP), 251
- Mayor, M., Pepe, F., Queloz, D., et al. 2003, *Msngr*, **114**, 20
- McCully, C., Volgenau, N. H., Harbeck, D.-R., et al. 2018, *Proc. SPIE*, **10707**, 107070K
- McQuillan, A., Mazeh, T., & Aigrain, S. 2014, *ApJS*, **211**, 24
- Millholland, S., Laughlin, G., Teske, J., et al. 2018, *AJ*, **155**, 106
- Morrison, S. J., Dawson, R. I., & MacDonald, M. 2020, *ApJ*, **904**, 157
- Mustill, A. J., Davies, M. B., & Johansen, A. 2015, *ApJ*, **808**, 14
- Nesvorný, D., & Vokrouhlický, D. 2016, *ApJ*, **823**, 72
- Parviainen, H. 2015, *MNRAS*, **450**, 3233
- Rein, H., & Liu, S. F. 2012, *A&A*, **537**, A128
- Rein, H., & Spiegel, D. S. 2015, *MNRAS*, **446**, 1424
- Salvatier, J., Wiecki, T. V., & Fonnesbeck, C. 2016, *PeerJ Computer Science*, **2**, e55
- Schneider, J., Dedieu, C., Le Sidaner, P., Savalle, R., & Zolotukhin, I. 2011, *A&A*, **532**, A79
- Smith, J. C., Stumpe, M. C., Van Cleve, J. E., et al. 2012, *PASP*, **124**, 1000
- Stumpe, M. C., Smith, J. C., Catanzarite, J. H., et al. 2014, *PASP*, **126**, 100
- Tamayo, D., Rein, H., Shi, P., & Hernandez, D. M. 2020, *MNRAS*, **491**, 2885
- Theano Development Team 2016, arXiv:1605.02688
- Thommes, E. W., & Lissauer, J. J. 2003, *ApJ*, **597**, 566
- Twicken, J. D., Catanzarite, J. H., Clarke, B. D., et al. 2018, *PASP*, **130**, 064502
- Van Eylen, V., Albrecht, S., Huang, X., et al. 2019, *AJ*, **157**, 61
- Wolff, S., Dawson, R. I., & Murray-Clay, R. A. 2012, *ApJ*, **746**, 171
- Zechmeister, M., & Kürster, M. 2009, *A&A*, **496**, 577